Available online at www.sciencedirect.com

SciVerse ScienceDirect

Ceramics International 39 (2013) 4819–4824

CERAMICS INTERNATIONAL

www.elsevier.com/locate/ceramint

Ablation mechanisms of interpenetrating Al20Si/graphite composites

Li Bing-qing*, Kang Peng-chao, Gou Hua-song, Zhang Qiang, Wu Gao-hui

School of Materials Science and Engineering, Harbin Institute of Technology, Harbin, Heilongjiang 150001, PR China

Received 27 September 2012; received in revised form 24 November 2012; accepted 25 November 2012
Available online 3 December 2012

Abstract

In order to utilize the latent heat of metal fusion and evaporation, Al20Si/graphite was added into graphite by squeeze casting infiltration. Its ablation properties were tested by oxy-acetylene flame. Compared with graphite, linear ablation rates of Al20Si/graphite decrease nearly by one order of magnitude. However, linear ablation rate of Al20Si/graphite increases with ablation time, which is caused by the change of ablation mechanism. At the beginning of ablation process, thermal chemical erosion plays an important part and thermal protective effect comes from the melting of Al20Si, the alleviation of liquid Al_2O_3 towards flame scouring and the decrease of porosities compared with graphite, while with ablation processing thermal mechanical erosion turns to dominate and thermal protective effect is mainly presented on the prevention of oxygen diffusion by the molten Al_4SiC_4 covered on ablation surface and the oxygen diffusion barrier effect of Al_4SiC_4 stuffed into graphite pores.

Keywords: B. Porosity; D. Carbides; Squeeze casting infiltration; Ablation mechanism

1. Introduction

With the rapid development of aerospace technology, the demand for advanced thermal protective materials continues increasing. Carbon-based materials have been considered to be one promising candidate materials for severe environments with super-high temperature and high pressure for their high temperature capability (over 2000 °C), high thermal shock resistance, good ablation resistance and low density [1–8]. However, the oxidation resistance of carbon is quite poor, which limits the further application of carbon-based materials in aerospace fields [8–11].

Refractory metal carbides or borides such as SiC, WC, ZrB_2, ZrC, TiC, TaC can be added into carbon matrix to improve its high temperature capability [8–16]. During the ablation process, the carbides or borides react with ablative atmosphere and form a liquid oxide layer on the ablation surface. The liquid oxide layer can prevent heat transfer and oxygen diffusion towards the interior of the composites to protect the matrix.

But one limitation of the idea above is that most of the refractory metal carbides are introduced into carbon by reaction metal infiltration (RMI) [11–15]. During the RMI process, molten metal reacts with carbon matrix and forms metal carbides. Therefore, these metal carbides/carbon composites fail to utilize the latent heat of metal fusion and evaporation during the ablation process.

Al has a priority to react with oxygen compared with carbon. Adding Al to carbon can utilize the latent heat of aluminium fusion and protect carbon from being oxidized at low temperature. And the formation of liquid aluminium oxide layer at higher temperature may protect carbon matrix from being oxidized. But if the composites only consist of Al and C, during the ablation process Al will react with carbon and forms Al_4C_3 after melting. Both Al_4C_3 and carbon can be easily oxidized by oxygen, thus the composites may present a low oxidation resistance. Considering that Al_4SiC_4 is one kind of promising high-temperature ceramics for its unique combination of the high melting point (~2080 °C), the low density (3.03 g/cm^3),

*Corresponding author. Tel.: +86 451 86402372; fax: +86 451 86412164.
E-mail address: libingqinghit@gmail.com (B.-q. Li).

0272-8842/$ - see front matter © 2012 Elsevier Ltd and Techna Group S.r.l. All rights reserved.
http://dx.doi.org/10.1016/j.ceramint.2012.11.072

excellent oxidation resistance and corrosion resistance [17–22], Si was added into the composites, too.

During the fabrication of the composites, the formation of Al_4C_3, which limits the utilization of the latent heat of Al fusion may do harm to the storage of Al–C composites as a result of hydrolysis in wet atmosphere, can be prevented when the concentration of Si is greater than 15%wt [23,24]. Thus, Al20Si was added into porous graphite by squeeze casting infiltration in this paper. The ablation properties and ablation mechanisms of Al20Si/graphite were also investigated.

2. Experimental

2.1. Preparation of Al20Si/graphite composites

The porous graphite XH-104 (manufactured by Nantong Xianghai Carbon Corporation, China) was used as the preform. Relevant properties of graphite are listed in Table 1. A named Al20Si (produced by Sichuan Lande Industry Corporation, China) was chosen as the infiltrated penetrant.

Al20Si/graphite composites were prepared by squeeze casting infiltration. The porous graphite preform and Al20Si alloy were together heated up to 800 °C in a vacuum hot pressing sintering furnace. Liquid Al20Si alloy was forced into porous graphite preform under a pressure of 12 MPa. Fast cooling measures were adopted to avoid the formation of Al_4C_3.

2.2. Ablation tests and microstructure analysis

The ablation properties of Al20Si/graphite were tested by oxy-acetylene flame. The size of the specimens was $\Phi 30 \times 10$ mm. The flux and pressure of oxygen and acetylene were 1512 L/h and 0.4 MPa, 1116 L/h and 0.095 MPa, respectively. The specimens were placed in a graphite fixture. The graphite fixture is 10 ± 0.02 mm from the nozzle with a diameter of 2 mm. The angle between oxy-acetylene flame and ablation surface was 90°. The heat flux was 4186.8 ± 418.68 kW/m^2 and the temperature of oxy-acetylene flame measured by optical pyrometer is about 2700–3000 °C. The ablation times were 5 s, 30 s and 60 s. At least 4 samples were tested for each ablation time. Linear ablation rate was calculated by the following formula:

$$R_l = \Delta l / \Delta t, \quad (1)$$

where R_l is linear ablation rate, Δl is the length change of the ablation centre and Δt is ablation time. The microstructure of Al20Si/graphite was investigated by transmission electron microscope (TEM, Philips CM12). The ablation morphologies of the composites were investigated by scanning electron microscope (SEM, Hitachi-S4800). Phase constitution of the composites was analysed by X-ray diffraction (XRD, Rigaku D/max-2400).

Table 1
Properties of XH-104 graphite.

Compression strength (MPa)	60.3
Flexural strength (MPa)	49.5
Ash content (%)	0.5
Porosity (vol%)	20.6
Most probable aperture (μm)	10.2
Volume density (g/cm^3)	1.7

3. Results and discussion

3.1. Microstructure of the composites

Fig. 1 shows the SEM image, TEM image and XRD pattern of interpenetrating Al20Si/graphite composites. As can be seen from Fig. 1a, the bright areas and the dark areas are Al20Si and graphite, respectively. Though some residual closed pores resulting from graphite production are visible on SEM morphology [25–27], most pores have been filled by Al20Si alloy homogenously. Fig. 1b presents the interface microstructure of Al20Si/graphite. Many graphite nanocrystals distribute separately on Al-graphite interface, which can be confirmed by the electron diffraction patterns. The selected area electron diffraction pattern from the nanocrystals presents four nanocrystalline rings, which are in accordance with (002), (100), (102) and (110) crystal planes of graphite. Though these graphite nanocrystals may become the nucleating centre of Al_4C_3, no Al_4C_3 was found on the interface according to both TEM and XRD results (Fig. 1c). This is attributed to the fast

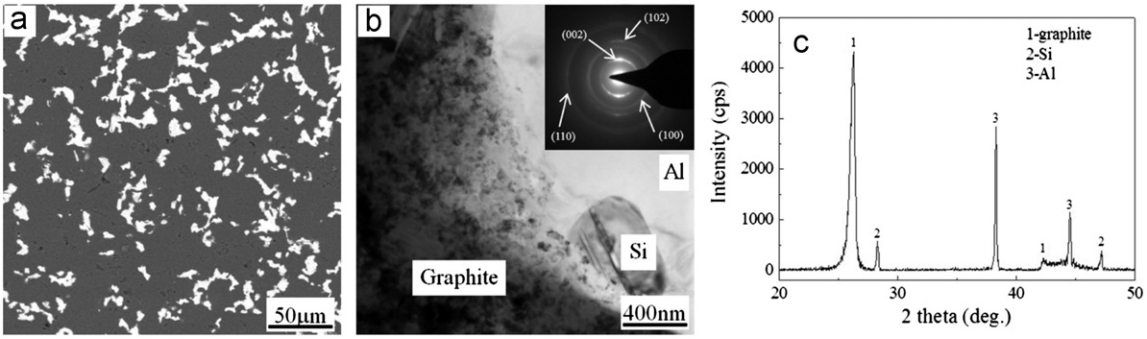

Fig. 1. SEM image (a), TEM image (b) and XRD pattern (c) of interpenetrating Al20Si/graphite composites.

cooling measurements. The phase constitution of Al20Si/graphite is Al, Si and graphite.

3.2. Ablation properties

Table 2 shows linear ablation rates of graphite and Al20Si/graphite composites. In the first 30 s, linear ablation rate of the graphite almost keeps constant, which is about 1×10^{-1} mm/s. During the following 30 s, ablation accelerates and linear ablation rate of the graphite increases to 2.082×10^{-1} mm/s, while linear ablation rate of the composites decreases nearly by one order of magnitude and is on the same magnitude with C/C-refractory metal carbides reported in the literature [11–15]. However, linear ablation rate of Al20Si/graphite dramatically increases with time: when the ablation time increases from 5 s to 60 s, linear ablation rate increases from 1.00×10^{-2} mm/s to 4.27×10^{-2} mm/s accordingly.

Table 2
Linear ablation rates of graphite and Al20Si/graphite ($\times 10^{-2}$ mm/s).

Ablation time	5 s	30 s	60 s
Graphite	10.00 ± 0.03	10.71 ± 0.05	20.82 ± 0.06
Al20Si/graphite	1.00 ± 0.05	2.07 ± 0.03	4.27 ± 0.07

3.3. Ablation mechanisms

Fig. 2 presents the macro- and micro-morphology of graphite ablated for 30 s. Fig. 2a shows that a big ablation pit forms on the ablation surface. The micropore sizes turns to be much larger than those before ablation, as is shown in Fig. 2b. Some of the micropores which are close to each other become connected. As is known to all, porosity has a significant effect on the ablation properties. First, materials with porosities have a relatively larger contact area with ablative atmosphere than those without porosities. Thus the ablation speed of materials with porosities will be much higher than those without porosities. On the other hand, ablative atmosphere can diffuse through pores and induce ablation inside the materials, which indirectly enhances the surface ablation. Furthermore, the edge of pores will be easily ablated by the high speed ablative atmosphere as a result of relatively sharp shape. Thus materials with porosities will be seriously ablated.

Fig. 3 shows the macro-morphologies of Al20Si/graphite specimens ablated for different time. The typical morphologies can be divided into three zones: central zone, transitive zone and marginal zone, as is shown in Fig. 3b and c. The boundary between transitive zone and marginal

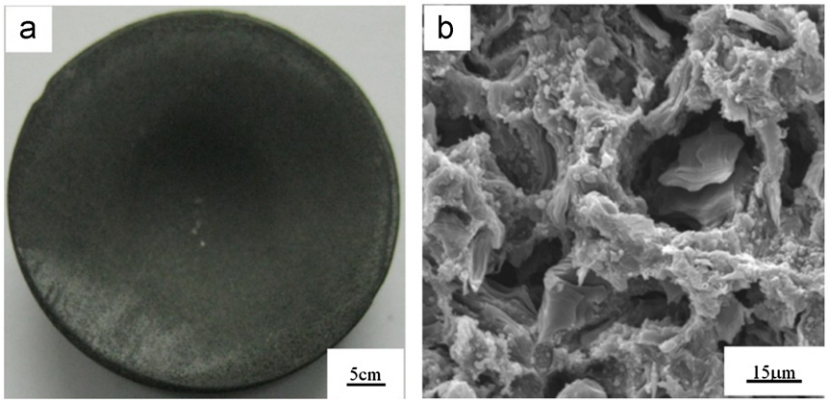

Fig. 2. Macro-ablation morphology (a) and micro-ablation morphology (b) of graphite ablated for 30 s.

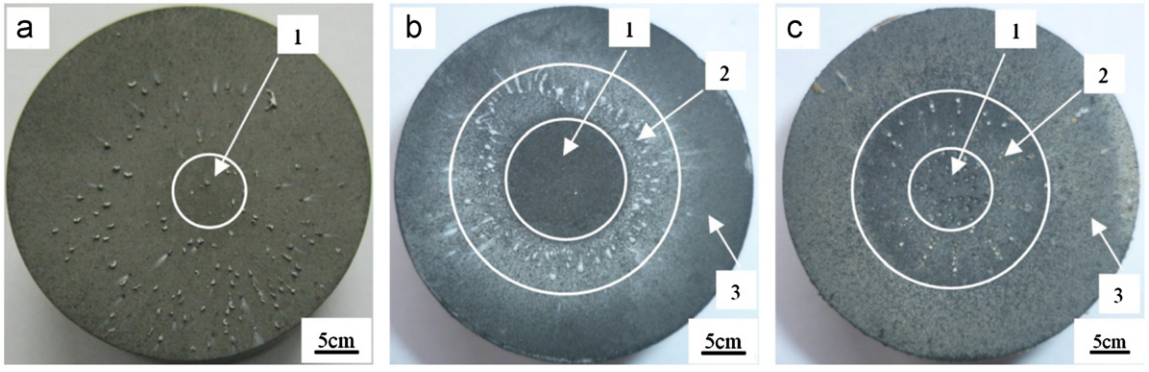

Fig. 3. Macro-morphologies of Al20Si/graphite specimens ablated for different time (1 central zone; 2 transitive zone; 3 marginal zone). (a) 5 s, (b) 30 s, and (c) 60 s.

zone of the specimen ablated for 5 s is not clear. Central zone directly contacts to oxy-acetylene flame and is ablated most seriously among three zones. The surface of central zone ablated for 5 s is still smooth but its colour is slightly darker than the other zones. During the first 5 s, Al20Si in central zone gushes out from graphite matrix, which increases the porosity in central zone. Thus the colour of central zone turns to be a little darker than other zones.

As for the specimen ablated for 30 s, central zone is a little lower than transitive zone and marginal zone. No macroscopic metal oxides can be observed on the surface of central zone. There are a lot of droplet-like metal oxides adhered to the surface of transitive zone, which verifies that metal oxides are molten during the ablation process. The droplet-like metal oxides are considered to form in central zone and then be scoured to transitive zone. Marginal zone is least ablated and thin metal oxide film can be observed.

When ablation time increases to 60 s, the surface of transitive zone turns to be quite coarse and small ablation pits form in central zone. So the ablation mechanism of ablation time for 60 s may be different from that of ablation time for 30 s.

Fig. 4 presents the micro-morphologies of central zone ablated for different time. As can be seen from Fig. 4a, central zone ablated for 5 s is covered by a layer of white substances and the porosity remarkably increases. At the beginning of the ablation process, infiltrated Al20Si melts and expands. The melting of Al20Si absorbs heat and slows down the temperature rise inside the composites. As a result of expansion of Al20Si, a pressure difference between composites inside and ablation environment is engendered and forces the molten Al20Si to gush out, which increases the porosity. Part of molten Al20Si further absorbs heat and quickly evaporates out as a result of high temperature (approximately 3000 °C). An EDS result shows the Al/O atom ratio of white substances covered on the surface is very close to 2/3 (Fig. 4b). Combined with the XRD results (Fig. 5), it can be concluded that the white substances are Al_2O_3 with a little Si. Since the formation of Al_2O_3 has consumed oxygen, graphite matrix is protected from oxidation. Meanwhile, as a transitive liquid layer between oxy-acetylene flame and ablation surface, Al_2O_3 can alleviate flame scouring towards graphite matrix. On the other hand, Al_2O_3 can prevent part of heat transfer and oxygen diffusion, thus the ablation resistance of Al20Si/graphite improves. But it can be also found out from Fig. 4a that the graphite matrix of central zone is still partly oxidized in despite the protection of Al_2O_3.

Al_4C_3 is also formed after ablating for 5 s according to XRD results (Fig. 5). As the gushing out of liquid Al20Si reduces the pressure difference between composites inside

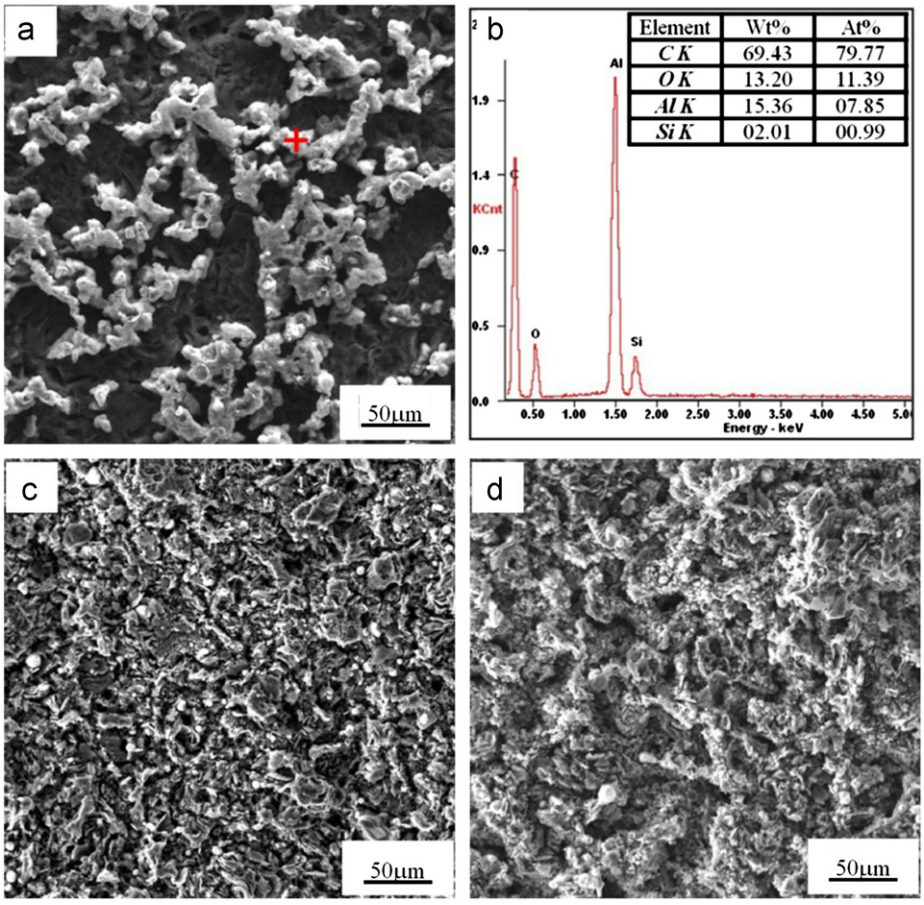

Fig. 4. Micro-morphologies of central zones ablated for 5 s (a), with its EDS spot pattern (b), 30 s (c), and 60 s (d).

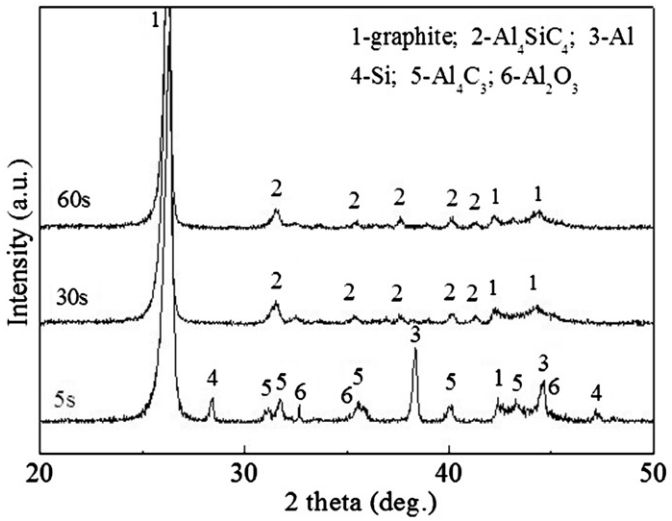

Fig. 5. XRD patterns of central zones ablated for different time.

and ablation environment, not all the molten Al20Si has enough driving force to transfer to ablation surface. Some residual Al20Si beneath the ablation surface will then react with graphite matrix and forms Al_4C_3 at high temperature. The formation of Al_4C_3 hinders the flowing of interior liquid Al20Si to the ablation surface and thus the formation amount of metal oxides decreases. Therefore, the thermal protection efficiency will reduce. However, compared with porous graphite, the stuffing of Al_4C_3 into graphite pores will prevent oxygen diffusion towards the composites and reduce ablation rate. In general, ablation of Al20Si/graphite at the beginning of ablation process mainly consists of the melting and oxidizing of Al20Si, as well as oxidizing of porous graphite. Thermal protective effect at the beginning of the ablation process is mainly caused by the melting and evaporating of Al20Si, the formation of Al_2O_3 and the stuffing of Al_4C_3 into graphite pores. However, which one of the three dominates the ablation resistance still needs further research.

With ablation time increasing to 30 s, the main phase constitution turns to be graphite and Al_4SiC_4 (Fig. 5). Al_4SiC_4 is obtained by the reaction among Al_4C_3, Si and graphite. The ablation temperature is much higher than the melting point of Al_4SiC_4, so Al_4SiC_4 is molten during the ablation process, which can be also confirmed by the ablation morphology (Fig. 4c). Since Al_4SiC_4 has excellent oxidation resistance and high chemical stability, less metal oxides can be found (Fig. 5). The molten Al_4SiC_4 covers on the ablation surface and protects graphite from oxidation. Besides, Al_4SiC_4 formed inside the composites will block the diffusion tunnel of ablative atmosphere and decrease the ablation inside the composites. In this ablation period, the content of Al20Si is little and less latent heat of Al20Si fusion can be used to resist ablation. Therefore, linear ablation rate of Al20Si/graphite ablated for 30 s dramatically increases to 2.07×10^{-2} mm/s. Ablation of Al20Si/graphite in this period mainly consists of oxidation and thermal mechanical erosion of graphite. Thermal protective effect in this period is mainly caused by the molten Al_4SiC_4 covered on the ablation surface and the stuffing of Al_4SiC_4 into graphite pores.

With ablation time increasing to 60 s, some ablation pits appear in central zone. SEM morphology of ablation pits bottom is shown in Fig. 4c. It can be seen that the morphology is much rougher than that ablated for 30 s, though the phase constitution is the same. Rough morphology increases aerodynamic heat and changes the distribution of heat flux on ablation surface. Small eddy currents are then formed, which lead to the formation of ablation pits and accelerate ablation. Thermal mechanical erosion turns to be more serious and becomes the main reason of ablation. Thus linear ablation rate of Al20Si/graphite ablated for 60 s significantly increases to 4.27×10^{-2} mm/s. Thermal protective effect still comes from the molten Al_4SiC_4 covered on the ablation surface and the stuffing of Al_4SiC_4 into graphite pores, which is the same with that of ablation time for 30 s.

4. Conclusions

Al20Si was added into porous graphite by squeeze casting infiltration to improve the ablation properties of graphite. After the addition of Al20Si, linear ablation rates decrease nearly by one order of magnitude. As ablation mechanism changes from thermal chemical erosion to thermal mechanical erosion with ablation processing, linear ablation rate of Al20Si/graphite significantly increases with ablating time.

At the beginning of ablation process, ablation of Al20Si/graphite is mainly caused by thermal chemical erosion, such as the melting and oxidation of Al20Si and the oxidation of porous graphite. Thermal protective effect mainly comes from the melting of Al20Si, the formation of Al_2O_3 and the stuffing of Al_4C_3 into graphite pores. With ablation time increasing, less latent heat of Al20Si fusion can be used. Thus the ablation resistance decreases. Thermal mechanical erosion of graphite turns to be the main reason of ablation. Thermal protective effect is then mainly caused by the molten Al_4SiC_4 covered on the ablation surface and the stuffing of Al_4SiC_4 into graphite pores.

Acknowledgement

This work was supported by National Natural Science Foundation of China under Project no. 90816017.

References

[1] M.M. Opeka, I.G. Talmy, J.A. Zaykoski, Oxidation-based materials selection for 2000 °C+ hypersonic aerosurfaces: theoretical considerations and historical experience, Journal of Materials Science 39 (2004) 5887–5904.
[2] D.L. Schmidt, K.E. Davidson, L.S. Theibert, Unique applications of carbon–carbon composite materials II, SAMPE Journal 35 (1999) 51–63.
[3] Donghwan Cho, Byung II Yoon, Microstructural interpretation of the effect of various matrices on the ablation properties of carbon-

fiber-reinforced composites, Composites Science and Technology 61 (2001) 271–280.
[4] J.C. Han, X.D. He, S.Y. Du, Oxidation and ablation of 3D carbon–carbon composite at up to 3000 °C, Carbon 33 (1995) 473–478.
[5] J.F. Huang, X.R. Zeng, H.J. Li, X.B. Xiong, G.L. Sun, ZrO_2–SiO_2 gradient multilayer oxidation protective coating for SiC coated carbon/carbon composites, Surface and Coatings Technology 190 (2005) 255–259.
[6] Y.L. Zhang, H.J. Li, Q.G. Fu, X.Y. Yao, K.Z. Li, G.S. Jiao, An oxidation protective Si–Mo–Cr coating for C/SiC coated carbon/carbon composites, Carbon 46 (2008) 179–182.
[7] J. Yin, X. Xiong, H.B. Zhang, B.Y. Huang, Microstructure and ablation performances of dual-matrix carbon/carbon composites, Carbon 44 (2006) 1690–1694.
[8] S.F. Tang, J.Y. Deng, W.C. Liu, K. Yang, Mechanical and ablation properties of 2D-carbon/carbon composites pre-infiltrated with a SiC filler, Carbon 44 (2006) 2877–2882.
[9] X.T. Li, J.L. Shi, G.B. Zhang, H. Zhang, Q.G. Gao, L. Liu, Effect of ZrB_2 on the ablation properties of carbon composites, Materials Letters 60 (2006) 892–896.
[10] J. Yin, H.B. Zhang, X. Xiong, B.Y. Huang, J.L. Zuo, Ablation properties of carbon/carbon composites with tungsten carbide, Applied Surface Science 255 (2009) 5036–5040.
[11] Yiguang Wang, Xiaojuan Zhu, Litong Zhang, Laifei Cheng, C/C–SiC–ZrC composites fabricated by reactive melt infiltration with $Si_{0.87}Zr_{0.13}$ alloy, Ceramics International 38 (2012) 4337–4343.
[12] Yonggang Tong, Shuxin Bai, Ke Chen, C/C–ZrC composite prepared by chemical vapor infiltration combined with alloyed reactive melt infiltration, Ceramics International 38 (2012) 5723–5730.
[13] Huilong Pi, Fan Shangwu, Yiguang Wang, C/SiC–ZrB_2–ZrC composites fabricated by reactive melt infiltration with $ZrSi_2$ alloy, Ceramics International 38 (2012) 6541–6548.
[14] Zhaoqian Li, Hejun Li, Shouyang Zhang, Kezhi Li, Microstructure and ablation behaviors of integer felt reinforced C/C–SiC–ZrC composites prepared by a two-step method, Ceramics International 38 (2012) 3419–3425.
[15] L.P. Ran, K. Peng, M.Z. Yi, L. Yang, Ablation property of a C/C–Cu composite prepared by pressureless infiltration, Materials Letters 65 (2011) 2076–2078.
[16] Y. Wang, Y.D. Xu, Y.G. Wang, L.F. Cheng, L.T. Zhang, Effects of TaC addition on the ablation resistance of C/SiC, Materials Letters 64 (2010) 2068–2071.
[17] J.F. Huang, X.R. Zeng, H.J. Li, X.B. Xiong, M. Huang, Al_2O_3–mullite–SiC–Al_4SiC_4 multi-composition coating for carbon/carbon composites, Materials Letters 58 (2004) 2627–2630.
[18] L. Solozhenko, O. Kurakevych, Equation of state of aluminum silicon carbide α-Al_4SiC_4, Solid State Communications 133 (2005) 87–89.
[19] K. Inoue, S. Mori, A. Yamaguchi, Thermal conductivity and temperature dependence of linear thermal expansion coefficient of Al_4SiC_4 sintered bodies prepared by pulse electronic current sintering, Journal of the Ceramic Society of Japan 111 (2003) 348–351.
[20] K. Inoue, A. Yamaguchi, S. Hashimoto, Fabrication and oxidation resistance of Al_4SiC_4 body, Journal of the Ceramic Society of Japan 110 (2002) 1010–1015.
[21] Xiaoxiao Huang, Guangwu Wen, Mechanical properties of Al_4SiC_4 bulk ceramics produced by solid state reaction, Ceramics International 33 (2007) 453–458.
[22] A.P. Luz, M.M. Miglioli, T.M. Souza, S. Hashimoto, S. Zhang, V.C. Pandolfelli, Effect of Al_4SiC_4 on the Al_2O_3–SiC–SiO_2–C refractory castables performance, Ceramics International 38 (2012) 3791–3800.
[23] T. Etter, P. Schulz, M. Weber, J. Metz, M. Wimmler, J.F. Loffler, et al., Aluminium carbide formation in interpenetrating graphite/aluminium composites, Materials Science and Engineering A 448 (2007) 1–6.
[24] R.Y. Lin, Interface evolution in aluminum matrix composites during fabrication, Key Engineering Materials 104–107 (1995) 507–522.
[25] T. Etter, J. Kuebler, T. Frey, P. Schulz, J.F. Loffler, P.J. Uggowitzer, Strength and fracture toughness of interpenetrating graphite/aluminium composites produced by the indirect squeeze casting process, Materials Science and Engineering A 386 (2004) 61–67.
[26] H. Mayer, M. Papakyriacou, Fatigue behaviour of graphite and interpenetrating graphite–aluminium composite up to 10^9 load cycles, Carbon 44 (2006) 1801–1807.
[27] T. Etter, M. Papakyriacou, P. Schulz, P.J. Uggowitzer, Physical properties of graphite/aluminium composites produced by gas pressure infiltration method, Carbon 41 (2003) 1017–1024.